Journal of
Materials Chemistry A

Materials for energy and sustainability

Accepted Manuscript

This article can be cited before page numbers have been issued, to do this please use: J. Shao, P. Dhakal, R. Intakul, X. H. Le, P. H. Ho, D. Creaser and L. Olsson, *J. Mater. Chem. A*, 2026, DOI: 10.1039/D6TA00954A.

ROYAL SOCIETY OF CHEMISTRY

rsc.li/materials-a

View Article Online
DOI: 10.1039/D6TA00954A

ARTICLE

H_2-SCR at high water concentrations with *in-situ* generated NH_3-SCR for efficient removal of NO_x from H_2 engines

Received 00th January 20xx,
Accepted 00th January 20xx

DOI: 10.1039/x0xx00000x

Jieling Shao,[a] Prabin Dhakal,[a] Rawipa Intakul,[a] Huy Xuan Le,[a] Phuoc Huang Ho,[a] Derek Creaser,[a] and Louise Olsson* [a]

The two main challenges of application of Pd-based catalysts in H_2-SCR are catalytic performance and water resistance. In this study, oxide supports (TiO_2 and ZrO_2) were employed and experimentally demonstrated to exhibit higher catalytic activity than the SSZ-13 zeolite-supported catalyst. Furthermore, doping Mn into Pd/TiO_2 further increased the maximum NO conversion to 61% compared to 44% for undoped Pd/TiO_2. Comprehensive characterization techniques, including XRD, STEM, XPS, CO-DRIFTS, and H_2-reduction experiments, were used to investigate the catalysts' physicochemical properties and hydrogen spillover behavior. $Pd/MnTiO_2$ not only maintained the strong metal-support interaction observed in Pd/TiO_2 but also significantly optimized the surface electronic structure. A higher proportion of metallic Pd facilitated H_2 dissociation and enhanced hydrogen spillover, leading to improved catalytic activity. Water resistance tests, at 5%, and up to 12% water vapor, revealed that the zeolite-supported catalyst exhibited superior tolerance to water. Although the oxide-supported catalysts were more sensitive to water, they still maintained significantly higher catalytic activity overall. Notably, $Pd/MnTiO_2$ exhibited the largest formation of NH_3. Finally, since NH_3 was identified as a major byproduct during H_2-SCR over $Pd/MnTiO_2$, a novel NOx removal strategy was developed by adding a downstream Cu-SSZ-13 monolith to establish an integrated H_2-SCR and NH_3-SCR reaction system. This configuration successfully increased the maximum NO conversion to 78%, with N_2 and N_2O as the only detected products, achieving a nitrogen selectivity of 76%.

Introduction

Hydrogen, as an alternative energy source, has garnered widespread attention in recent years. It has been reported that while internal combustion engines (ICE) using fossil fuels contribute 25% of the world's power, they are also responsible for more than 10% of global greenhouse gas emissions (GHGs) [1]. In addition, conventional ICEs not only produce GHGs (CO_2, N_2O, etc) but also other harmful gases (CO, NO_x, etc) and particulate matter, which need to be removed via catalytic techniques. Therefore, clean hydrogen can play an important role in utilizing internal combustion engines [2-4]. Although the combustion of hydrogen produces water, the combustion process is accompanied by a small amount of NO_x emissions because air, rather than pure oxygen is used in ICEs. The development of hydrogen internal combustion engines (H_2-ICEs) has made selective catalytic reduction of NO_x using hydrogen (H_2-SCR) an attractive alternative to conventional NH_3-SCR catalysts in exhaust after-treatment systems. This is because hydrogen is already available onboard as fuel in emerging H_2-ICE platforms, such as the Cummins X15H heavy-duty engine, MAN hydrogen-powered trucks, and JCB hydrogen-fueled off-road machinery engine, as described in their webpages.

In many studies, Pt and Pd are considered as the active centers for the H_2-SCR under lean-burn conditions, offering a high potential for low-temperature emission reductions [5, 6].Our previous study showed that NO reduction with hydrogen can also occur at high temperatures using an Ir catalyst, which covers a wide temperature window with combinations of catalysts [7]. Pd showed a moderate active temperature window and a relatively high N_2 selectivity. However, one challenge in developing Pd-based catalysts for H_2-SCR is their lower activity compared to Pt catalysts [8-10] . To address this, researchers have applied some effective strategies. Deutschmann and co-workers successfully boosted the activity of Pd-based catalysts for H_2-SCR by using a combination of oxides and zeolite ($20\%TiO_2$/HY and $5\%V_2O_5/20\%TiO_2$-Al_2O_3) supports [11]. Liu et al. added Mn as a dopant to modify Pd/TiO_2-Al_2O_3, which not only enhanced activity but also remarkably increased N_2 selectivity above 150 °C. They revealed that new active nitrogen oxides formed on MnO_x, which are unstable and more active [12].Yang's group investigated the effect of a nickel additive on Pd/TiO_2 for H_2-SCR, revealing the synergistic effects between Pd and Ni promoted catalytic activity and N_2 selectivity [13]. They also noted that adding Ni altered the profiles of H_2 adsorption and spillover from the Pd/TiO_2. As a part of the H_2-SCR process, hydrogen spillover effects (HSPE) have been reported to be an interfacial phenomenon that plays a crucial role [14-18]. Peng et al. have demonstrated that enhanced hydrogen spillover could effectively eliminate the 'volcano-type' behavior of NO_x conversion vs. temperature in H_2-SCR over Pd-based catalysts [19]. Despite this, many scholars have noted that a comprehensive understanding of HSPE is still lacking, leading to debates about non-reducible oxide supports. Precious metals (Pt and Pd) are considered the most effective catalysts for the HSPE[20]. Additionally, researchers have found that hydrogen spillover is

[a] Chemistry and Chemical Engineering, Competence Centre of Catalysis, Chalmers University of Technology, SE-412 96 Gothenburg, Sweden.

View Article Online
DOI: 10.1039/D5TA00854A

influenced by particle size, the distribution of the noble metal, the type of support, and the interaction between metal and support.

Apart from the intrinsic performance of the catalyst, the high water content in the exhaust of hydrogen-powered vehicles presents a significant challenge that cannot be overlooked in the development of after-treatment catalysts. Water is the main combustion product, and its concentration in the exhaust depends on the air-fuel ratio (λ). It has been reported that at λ=1, the molar fraction of water is 34% for H_2-ICE [21, 22].This elevated water concentration has a significant impact on catalyst aging. The effect of water has been proven to have a divergent influence on the reaction by researchers. Costa et al. found a promoting effect of H_2O on Pt/MgO-CeO_2, because the dissociation of H_2O contributes to an increased H-reservoir and facilitates hydroxylation of the surface. As a result, N_2 selectivity was improved with more active NO_x species formed on the hydrated surface [23-25]. Xu et al. claimed a positive effect of H_2O on a Co-$Al_{1.95}Pd_{0.05}O_4$ catalyst, as the H_{ads} dissociated by H_2O could assist NO dissociation, improving N_2 formation [26]. However, water has a strong inhibitory effect on N_2 selectivity when 5% H_2O is added to the NO/H_2/O_2 feed on Pt/SiO_2 and Pt/Al_2O_3 catalysts due to the competitive chemisorption of NO and H_2O on the active site [27]. The inhibition and deactivating effect of H_2O was reported to be both reversible and irreversible, depending on the conditions. Severe deactivation occurs at high temperature, especially with higher water content, where the dispersion of active metals could decrease, as well as the surface area and pore volume. For the cases where zeolites are used as support, dealumination of the framework could occur [28]. Most studies have investigated the effect of water on H_2-SCR catalysts at concentrations up to 5% [29]. However, the application of H_2-ICE highlights the need to develop efficient H_2-SCR catalysts under conditions with elevated water content.

This study addresses two major challenges: enhancing catalytic activity and water resistance. In addition, we propose a novel strategy with *in-situ* generation of NH_3 during lean H_2-SCR and utilizing the formed NH_3 in a second catalyst. Briefly, we examined Pd on different supports and found that the H_2-SCR performance was significantly enhanced when using Mn-doped TiO_2. The crucial hydrogen spillover process was facilitated, which was thoroughly investigated and experimentally validated. Moreover, this study evaluated the catalytic performance of Pd catalysts under high humidity conditions (up to 12% water content) in the H_2-SCR process - a scenario rarely focused on in previous studies. To effectively utilize the by-product NH_3 generated from the H_2-SCR, an innovative hybrid post-treatment strategy that integrates an NH_3-SCR catalyst after was proposed. This approach led to an increase in NO conversion up to 78%, and an improvement in N_2 selectivity to around 76%.

Experimental

Catalyst preparation

H-SSZ-13 zeolite preparation

Na-SSZ-13 (Si/Al=9.5) was lab-synthesized with a hydrothermal method [30]. The details of the synthesis of Na-SSZ-13 is written in the supplementary information (SI). The product was obtained after the hydrothermal reaction at 160 ℃ for 6 days in a Teflon-lined stainless-steel autoclave and washed with Milli-Q water. It was dried at 80 ℃ for 12 h and calcined at 600 ℃ for 8 h to remove the organic template. The Na-SSZ-13 powder was collected and ion-exchanged with 0.5 M NH_4NO_3 solution (Thermo Scientific) at 80 ℃ for 2 h, during which 400 mL of solution containing 4 g of zeolite powder was thoroughly stirred. It was then washed with Milli-Q water, and the solids were separated from the liquid using a centrifuge. The ion-exchange and washing process was repeated twice. Afterward, the H-form SSZ-13 sample was obtained after drying in an oven at 80 ℃ for 12 h, followed by calcining at 550 ℃ for 6 h.

Pd-based catalysts (Pd/SSZ-13, Pd/TiO_2, Pd/ZrO_2) preparation

1 wt% of Pd was loaded onto various supports (H-SSZ-13, TiO_2 and ZrO_2) using an incipient wetness impregnation technique. A Pd solution was prepared by mixing the $Pd(NO_3)_2$ precursor (Alfa Aesar 10% Pd) with Milli-Q water. Titanium oxide (400 mesh powder ground from pellets) and zirconia oxide (UEP-100) were commercially purchased from Zeolyst and Daiichi Kiegnso Kagaku Kogyo, respectively. The wet volume of each support was determined using N_2 physisorption. The Pd solution was dropped into the carrier in batches, accompanied by grinding with a pestle to achieve a homogeneous distribution [31].The impregnated sample was dried in an oven at 80 ℃ for 12 h and then calcined at 550 ℃ for 8 h. The prepared catalysts were systematically labelled, with the active metal (Pd) indicated before the slash, and the corresponding support specified after the slash (Pd/SSZ-13, Pd/TiO_2, Pd/ZrO_2).

Mn modified catalyst (Pd/$MnTiO_2$) preparation

Mn was introduced as a metal promoter to modify the Pd/TiO_2 catalyst. The Pd/$MnTiO_2$ catalyst was prepared using a two-step incipient wetness impregnation method [12]. First, 1 wt% Mn was loaded onto TiO_2 powder using manganese (II) nitrate hydrate ($Mn(NO_3)_2{\cdot}6H_2O$, Sigma-Aldrich) as the Mn precursor. Specifically, 4 g of TiO_2 support was impregnated with 0.21 g of $Mn(NO_3)_2{\cdot}6H_2O$ to obtain a Mn loading of 1 wt%. After drying at 120 ℃ for 12 h, the resulting powder was used as the support for Pd. Subsequently, 1 wt% Pd was introduced using the same impregnation approach. In this step, 0.4 g of $Pd(NO_3)_2$ solution (10% Pd) was impregnated onto 4 g of $MnTiO_2$ to obtain a Pd loading of 1 wt%. Since the Pd loading was identical to that of the other Pd-based catalysts, the catalyst was labelled Pd/$MnTiO_2$, where Pd denotes the active metal and $MnTiO_2$ represents the Mn-modified TiO_2 support. Finally, the catalyst was subjected to the same drying and calcination procedures as the other samples. 2 wt% Cu/SSZ-13 was synthesized using an ion-exchange method [32, 33] and was placed downstream from the 1 wt% Pd/$MnTiO_2$ to utilize the ammonia produced from the Pd/$MnTiO_2$ catalysts during H_2-SCR for further NO_x reduction.

View Article Online DOI: 10.1039/C6TA09445B

Washcoating process

The powder catalyst was then dispersed in a mixture of 50 wt% ethanol and 50 wt% Milli-Q water, along with 5 wt% boehmite binder (Disperal P2, Sasol) to make a slurry. This slurry was stirred at room temperature for 12 h. The slurry was then coated onto a honeycomb monolith substrate (cordierite, D*L=1.5 cm*2.0 cm, 400 cpsi) until reaching the target loading of 300 mg. The monolith was dried in an oven at 80 ℃ for 12 h and calcined at 500 ℃ for 2 h after coating [34]. The wash-coated monolith was stored and ready for activity measurements.

Activity measurements

Activity test cycles were performed with a laboratory-scale flow reactor (synthetic gas bench, SGB). The monolith sample was inserted into a horizontal reactor tube with heating insulation. The inlet gas mixture was regulated by Bronkhorst mass flow controllers (MFCs), and water vapor was controlled by an evaporation and mixing system (CEM, Bronkhorst). The outlet gas composition was measured and monitored by FTIR (MKSTM Multigas 2030) and mass spectroscopy (Hiden HPR-20 QIC). It should be noted that the N_2 concentrations reported in ppm in the results and SI sections are based on calculations from FTIR data of NO, N_2O, NO_2 and NH_3, assuming 100% mass balance. The detailed test procedure and the reaction conditions are shown in **Table 1**. A pretreatment of the catalyst was the first step to stabilize the catalyst's state. The temperature was thereafter lowered to 80 ℃ and maintained for 90 min before starting the feed of the reaction gas mixture. The total flow was kept at 1200 NmL/min in an Ar balance. The cycle test consisted of a continuous warming and cooling process from 80 ℃ to 500 ℃ with a reaction gas composition of 500 ppm NO, 5000 ppm H_2, 10% O_2, and 5-12% H_2O. Each test cycle was repeated four times. The test results discussed in the paper were selected from the fourth cycle.

Table 1 The activity test cycle procedure and reaction conditions (GHSV=20,000 h^{-1} (STP)).

Step	H_2-SCR Experiment	Conditions
1	Pretreatment	(i) 10% O_2 and 5% H_2O in Ar for 4 h at 550 ℃
2	Cooling	(i) Cooling from 500 ℃ to 80 ℃ in Ar (rate: 5 ℃/min) (ii) keep at 80 ℃ for 90 min
3	Test cycle *4	(i) Continuous reaction from 80 ℃ to 500 ℃ (heating rate: 5 ℃/min) in the gas mixture of 500 ppm NO, 5000 ppm H_2, 10% O_2, 5-12% H_2O in Ar (ii) keep at 500 ℃ with the same gas mixture for 30 min (iii) continuous reaction from 500 ℃ to 80 ℃ (cooling rate: 5 ℃/min) in the same gas mixture and keep at 80 ℃ for 90 min.

Characterization methodology

The element analysis was measured with inductively coupled plasma sector field mass spectrometry (ICP-SFMS) by ALS Scandinavia (Luleå, Sweden). The surface area and pore structure parameters were determined with the Brunauer-Emmett-Teller and t-plot methods by N_2 physisorption (Micromeritics Tristar Ⅱ 3000 Analyzer). The catalyst's crystalline structure was measured by powder X-ray diffraction (XRD) using a Bruker AXS D8 Advance. The metallic particle dispersion and mean size were determined by CO chemisorption and high-resolution transmission electron microscopy (HRTEM). HRTEM was performed on an FEI Titan 80-300 microscope equipped with a high-angle annular dark-field (HAADF) detector. Particle size analysis was conducted with the software DigitalMicrograph.

CO chemisorption measurements were performed using an ASAP2020 Plus instrument (Micromeritics). Approximately 0.1 g of powder catalyst was reduced in 1% hydrogen at 400 ℃ for 1 h. The adsorption isotherms of CO were measured at intervals of 25 mmHg from 100 to 600 mmHg at 35 ℃.

The oxidation state of Pd was determined by X-ray photoelectron spectroscopy (XPS) analysis using a PHI5000 VersaProbe Ⅲ Scanning XPS MicroprobeTM with an X-ray source of monochromatic Al Kα radiation (Hv=1486.6 eV). Data analysis was based on the calibration of the adventitious carbon peak (C1s) at 284.8 eV using Multipak software. A survey scan was first performed for all the samples to identify the elements in the material within the range of 0-1100 eV. Subsequently, a fine scan of Pd was performed 15 times in the range of 330-348 eV in high power mode to improve the accuracy of the spectrum due to the low loading. Since the Zr 2p and Pd 3d lines overlapped, the narrow scan range was expanded to 320-358 eV. The XPSPEAK41 software was employed for fitting the spectrum and data analysis.

The surface chemistry and molecular interactions on the catalyst powder under different gas atmospheres were studied using *in-situ* diffuse reflectance infrared Fourier-transform spectroscopy (DRIFTS) spectra (Bruker Vertex 70 spectrometer). The outlet gases were measured by a mass spectrometer (Hiden HR20). In the first study of CO adsorption, 1000 ppm of H_2 in a total Ar balanced flow of 100 NmL/min was passed through at 250 ℃ to reduce the sample. After that, the temperature was cooled to 35 ℃, while exposing the sample to Ar only, to take a background spectrum. 1000 ppm CO/Ar was introduced over the sample for 60 min, and spectra were collected every 1 min. A pure Ar stream was then introduced for 1 h to observe the weaker desorption of CO species. The second study focused on the H_2-SCR without water on the Pd catalysts. In these experiments, the pretreatment was done under 10% O_2 at 300 ℃ for 30 min. Thereafter, the temperature was lowered to 80 ℃, while flushing with Ar, to collect the background spectrum. Then, a 500 ppm NO/Ar purge was passed through for 60 min. 2000 ppm H_2 was then introduced for 60 min, which could react with the NO_x species adsorbed on the catalyst surface. Thereafter, a fresh sample was loaded and pretreated at 300 ℃ with 10% O_2/Ar. The system was cooled to 80 ℃, while flushing in Ar, and the background spectrum was recorded. Following 500 ppm NO exposure for 1 h, 1% H_2O was added to the 500 ppm NO and kept flowing for another 1 h. Finally, the feed was switched to 2000 ppm H_2 with 1% H_2O for 60 min.

A differential scanning calorimeter (Sensys DSC calorimeter, Setaram) was used to detect the hydrogen spillover phenomenon. Yellow-colored WO_x was obtained by calcining

View Article Online
DOI: 10.1039/D6TA00054A

ammonium metatungstate hydrate (Sigma-Aldrich) at 500 ℃ for 5 h. Approximately 20 mg of catalyst powder mixture (catalyst/WO_x = 1/8 mass ratio) was loaded inside a quartz tube and plugged with quartz wool. 1 vol% H_2/Ar in a total flow of 20 NmL/min was introduced into the sample for 1 h after the temperature was elevated to 200 ℃. The outlet gases were measured with a mass spectrometer. The samples after H_2 reduction were compared to observe the color change, since WO_x is yellow, while H_xWO_3 which is formed during reduction is blue.

Temperature-programmed desorption of ammonia (NH_3-TPD) was conducted using the same setup. Initially, the catalyst samples were pretreated with 20 Nml/min Ar at 300 ℃ for 1 h. Following that, 2000 ppm of NH_3/Ar with a total flow of 20 NmL/min at 100 ℃ was added for 2 h until NH_3 was saturated on the sample. Then, an Ar flow was used to purge the physisorbed NH_3, and the temperature was elevated to 700 ℃ at a ramping rate of 10 ℃/min in pure Ar for examining the ammonia desorption. The outlet gas was measured and monitored by a mass spectrometer (Hiden, HPR-20 QIC). The acidity analysis was performed using an area integration method compared with the calibration of NH_3.

Results and discussion

Catalyst characterization

After loading 1 wt% Pd on the support (SSZ-13, TiO_2, $MnTiO_2$, and ZrO_2), their original crystal structures were maintained (**Fig. S1**). All the XRD patterns were compared and confirmed with the reference patterns (Baddeleyite_ZrO_2 #37-1484, Anatase_TiO_2 #21-1272, and chabazite_CHA #89-0735) [35]. **Fig. S1** also shows the XRD peak positions of PdO particles. Only the first characteristic peak of PdO around 34° can be faintly observed in the Pd/SSZ-13 and the two TiO_2 samples, indicating that Pd primarily exists in the form of oxides on the support surface. The physical properties of each sample are listed in **Table 2**. Unlike the three metal oxide supports, SSZ-13, as a small-pore zeolite, has the largest surface area of 613.8 m^2/g and the smallest pore size [36]. Due to its complex three-dimensional topological structure, it possesses a large pore volume [37] (0.43 cm^3/g).

The mean particle sizes of Pd were measured by TEM (**Table 2**), except for Pd/SSZ-13 where CO chemisorption was used. Clearly, Pd/SSZ-13 exhibited the smallest particle size compared to the others. For the oxide-supported catalysts, 50-100 randomly selected particles were measured to calculate Gaussian distributions and generate histograms, embedded in **Fig. 1**. In **Fig. 1d**, HRTEM mode was used for Pd/ZrO_2 instead of HAADF-STEM due to the close atomic numbers of Pd and Zr, making it difficult to clearly distinguish them based on brightness contrast in dark-field. Particle sizes calculated from TEM images were 16.6 nm for Pd/TiO_2, 11.8 nm for Pd/$MnTiO_2$, and 12.6 nm for Pd/ZrO_2.

Both XRD and BET results show no significant differences between Pd/TiO_2 and Pd/$MnTiO_2$ catalysts. However, **Fig. 1b** and **Fig. 1c** demonstrate a decreased Pd particle size with the addition of Mn on the TiO_2 support. The introduction of MnO_x could structurally increase the surface heterogeneity by creating additional facets and anchoring sites, thereby effectively separating Pd species [38]. Numerous studies have confirmed a synergistic effect between Pd and manganese oxides [12, 39]. This synergy suggests that the interactions between Pd and Mn oxides, particularly through Pd-O-Mn interfacial structures [40] play a key role in stabilizing Pd species and suppressing their surface migration and aggregation during synthesis and pretreatment. As a result, the Pd/$MnTiO_2$ catalyst exhibits smaller Pd particle sizes and improved dispersion compared with the unmodified Pd/TiO_2 catalyst.

Table 2 Physical properties of 1 wt% loaded Pd-based catalysts.

	Pd (wt%)	Surface Area (m^2/g)	Pore Volume (cm^3/g)	Mean particle size (nm)
Pd/SSZ-13	0.80	613.8	0.43	1.7*
Pd/TiO_2	0.88	30.9	0.13	16.0**
Pd/$MnTiO_2$	0.71	28.8	0.12	11.8**
Pd/ZrO_2	1.10	62.0	0.26	12.6**

*Particle size of Pd/SSZ-13 is measured from CO chemisorption.

**Particle was measured with TEM.

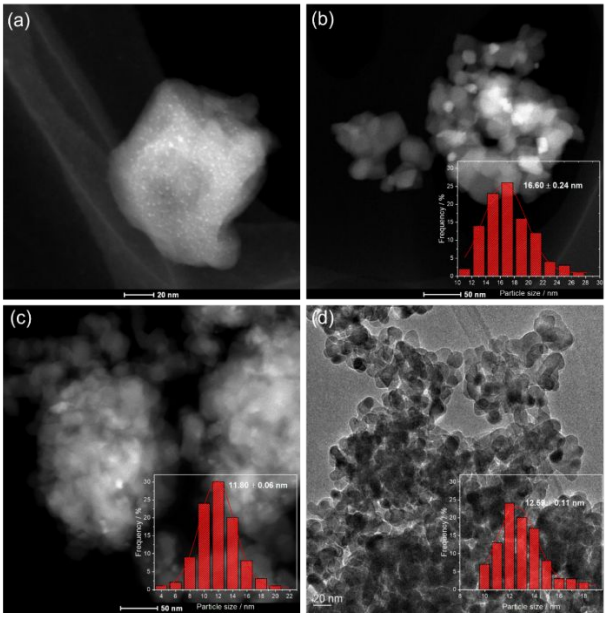

Fig. 1 HAADF-HRTEM images of (a) 1 wt% Pd/SSZ-13, (b) 1 wt% Pd/TiO_2, (c) 1 wt% Pd/$MnTiO_2$, and (d) 1 wt% Pd/ZrO_2 catalysts and Pd particle size distributions on Pd/metal oxide catalysts.

The oxidation states of Pd in the four catalysts were determined by X-ray photoelectron spectroscopy. The peak deconvolution and fitting are shown in **Fig. 2**, and the corresponding results are listed in **Table 3**. The binding energies near 336.5 eV and 341.75 eV (with a fixed separation of 5.26 eV) correspond to the $Pd3d_{5/2}$ and $Pd3d_{3/2}$ peaks of Pd^{2+} species, with a fixed peak area ratio of 3:2 [41]. Another pair of peaks at 338.0 eV and 343.3 eV is attributed to Pd^{4+} species. Therefore, Pd exists as both Pd^{2+} and Pd^{4+} in the Pd/ZrO_2 and Pd/SSZ-13 catalysts following the oxidative pretreatment. It is noteworthy that there is significant overlap between the Zr3p and Pd3d peaks within the same binding energy

View Article Online
DOI: 10.1039/D6TA00954A

range, which may affect spectral interpretation. For the Pd/SSZ-13 sample, about 80.5% was assigned to PdO_2 oxides, however it should be noted that the noise level is high (grey dotted line in Fig.2), which could be due to the low palladium loading in combination with ion-exchanged Pd.

The XPS results provide strong support for the strong metal-interaction (SMSI) effect on the TiO_2-support catalysts. TiO_2's reducibility can lead to the encapsulation of metal particles, interpenetrated as a charge transfer from the support to the dispersed metal [42-44]. Instead of the Pd^{4+} peaks, a pair of peaks appeared at much lower binding energies of 335.3 eV / 340.6 eV and 335.4 eV / 340.8 eV, which were assigned to Pd^0 species [43, 45, 46]. These findings indicate that even after an oxidative pretreatment, 31.8% of Pd remained in the metallic state (Pd^0) in the Pd/TiO_2 catalyst, which could be due to the SMSI effect, which limits oxygen adsorption on the Pd surface. Upon doping with Mn, the proportion of metallic Pd even further increased to 46.7%. In addition to changes in Pd oxidation states, a shift in the valence state of Ti was also observed in **Fig. S2**. As shown in **Table S1**, Pd/TiO_2 contained approximately 78.1% of Ti^{4+} and 21.9% of Ti^{3+}, whereas after Mn doping, the composition shifted to 42.7% of Ti^{3+} and 57.3% of Ti^{2+} [47]. This observation is consistent with previous studies reporting that Mn partially substitutes Ti in the TiO_2 lattice.[48-50] The substitution of Ti^{4+} by Mn^{2+} introduces a charge imbalance, which is compensated for by the formation of oxygen vacancies. As a result, Ti, that was originally coordinated with lattice oxygen is reduced to lower oxidation states. This mechanism was summarized by Nguyen *et al.* as follows[50]:

$$Ti^{4+} + e(O^{2-})Mn^{2+} \rightarrow Ti^{3+} + Oxygen\ vacancies + Mn^{2+}$$

To further support this interpretation, additional O1s XPS spectra were analyzed (**Fig. S3**). Two main peaks were observed at 529.4-529.6 eV and 531.1-531.3 eV, which are attributed to lattice O^{2-} in TiO_2 and oxygen vacancies or absorbed oxygen species, respectively [51-53]. It should be noted that an alternative interpretation assigns the O1s signal in the 531–532 eV range to surface hydroxyl groups formed from ambient water [54]. In the present study, the enhanced intensity of the peak at 531.3 eV is primarily attributed to an increased concentration of oxygen vacancies induced by Mn substitution and the associated charge-compensation effects. Meanwhile, the decreased intensity of the lower binding energy peak suggests a reduction in lattice oxygen. Moreover, both oxygen peaks exhibit a shift of approximately 0.2 eV toward higher binding energies, confirming that Mn incorporation alters the local electronic environment, leading to a partial reduction of both Pd and Ti species[55, 56].

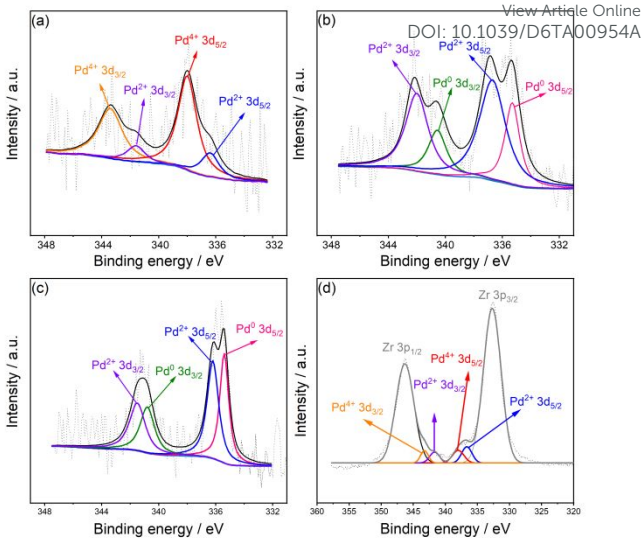

Fig. 2. X-ray photoelectron spectra of Pd3d in (a) 1 wt% Pd/SSZ-13, (b) 1 wt% Pd/TiO_2, (c) 1 wt% $Pd/MnTiO_2$, (d) 1 wt% Pd/ZrO_2 catalysts.

Table 3. X-ray photoelectron spectroscopy results of Pd3d in the catalysts.

Sample	Pd^0		Pd^{2+}		Pd^{4+}	
	BE/eV ($3d_{5/2}/3d_{3/2}$)	Fraction/ %	BE/eV ($3d_{5/2}/3d_{3/2}$)	Fraction/ %	BE/eV ($3d_{5/2}/3d_{3/2}$)	Fraction/ %
Pd/TiO_2	335.3/340.6	31.8	336.7/342.0	68.2		
$Pd/MnTiO_2$	335.4/340.8	46.7	336.2/341.5	53.3		
Pd/ZrO_2			336.7/341.7	53.8	338.0/343.3	46.2
Pd/SSZ-13			336.4/341.6	19.5	338.0/343.4	80.5

The acid properties of the catalysts were determined using NH_3-TPD (**Fig. S4**). It is evident that the SSZ-13 support exhibits by far the highest acid site density and the strongest acidity, as indicated by NH_3 desorption occurring with two desorption peaks at 205 °C and 425 °C, respectively. Desorption of NH_3 over 400 °C suggests strong adsorption binding of NH_3, typically associated with Brønsted acid sites [57]. Therefore, it can be inferred that SSZ-13, due to its stronger acidity, is capable of storing ammonia, possibly generated during the H_2-SCR process. In addition, the desorption peaks observed between 100–300 °C are attributed to weakly bound ammonia, which generally originates from Lewis acid sites. Among the metal oxide-supported catalysts, ZrO_2 exhibits a slightly higher concentration of Lewis acid sites compared to the TiO_2-supported catalysts. This also implies that catalysts supported by oxides with weaker acidity tend to store less ammonia, which will be further discussed in relation to catalytic performance.

Hydrogen spillover effect

The hydrogen spillover effect on the catalysts was determined using the same equipment as for NH_3-TPD. This phenomenon was

View Article Online
DOI: 10.1039/D5TA08054A

investigated by reducing a mixture of yellow-colored WO_3 with the catalyst sample. The hydrogen spillover leads to the formation of blue H_xWO_3 after the reduction treatment, applying the method developed by Yu et al. [58]. Among the three oxide-supported catalysts, Pd/TiO_2 and Pd/SSZ-13 exhibited the lightest colors (**Fig. S5a**), indicating the weakest H spillover effect. However, the addition of Mn to Pd/TiO_2 enhanced the spillover, as evident by a darker blue color. The redox activity of Mn (Mn^{2+}, Mn^{3+}, Mn^{4+}) modulates the surface structure and electronic properties of TiO_2. From an electronic perspective, Mn incorporation promotes the formation of a higher fraction of metallic Pd specie, as supported by XPS results. From a structural perspective, the introduction of Mn creates a more heterogeneous surface and, due to the sequential impregnation method in which Mn is loaded onto TiO_2 prior to Pd, can spatially separate Pd species from the TiO_2 surface. This partial separation may weaken the strong metal-support interaction (SMSI) between Pd and TiO_2, thereby reducing the encapsulation or coverage of Pd by TiO_2 overlayers. Therefore, the increased fraction of metallic Pd promotes H_2 dissociation, while the modified surface structure facilitates the migration of hydrogen atoms. Additionally, Zhou et al. have revealed that H spillover is more pronounced on smaller Ru particles [59]. As **Fig. 1** demonstrates, Mn addition improved Pd dispersion and reduced particle size on TiO_2, which likely contributed to the enhanced spillover. The Pd/ZrO_2 sample showed an intermediate color, suggesting a moderate spillover effect. The mechanism of H spillover differs between non-reducible zeolites and reducible metal oxides such as TiO_2 and ZrO_2 [15]. On zeolites, the process is primarily governed by the conjugated interaction between Brønsted (BAS) and Lewis (LAS) acid sites. In contrast, hydrogen migration over oxide supports proceeds through the transfer of H/H pairs between LASs. In addition, due to the unique microporous structure of zeolites, hydrogen spillover is inherently restricted and localized [60, 61]. Due to the relatively small color differences among the samples in **Fig. S5a**, the RGB color components were extracted, and the average proportion of the blue channel was quantitatively calculated (**Fig. S5b**). The resulting blue fractions for the four catalysts are 58% for Pd/SSZ-13, 72% for Pd/ZrO_2, 68% for Pd/TiO_2, and 74% for $Pd/MnTiO_2$.

CO adsorption was examined on the surfaces of the three oxide-supported catalysts, with spectra collected after 60 min of CO exposure as shown in **Fig. 3**. For the Pd/ZrO_2 catalyst, peaks were observed at 2085 cm^{-1}, 1980 cm^{-1}, 1930 cm^{-1}, 1630 cm^{-1}, 1568 cm^{-1}, 1425 cm^{-1}, 1340 cm^{-1}, and 1220 cm^{-1}. The IR peaks can be grouped into two regions: 2085-1930 cm^{-1}, corresponding to CO adsorbed on Pd species, and 1630-1220 cm^{-1}, corresponding to CO adsorbed on the oxide supports in various forms. The band at 2085 cm^{-1} is attributed to terminal carbonyls adsorbed on the Pd^0 defects [62, 63]. The peak at 1930 cm^{-1} corresponds to bridge-bonded CO on Pd (111) planes, while the 1980 cm^{-1} peak likely arises from CO adsorbed on Pd facets or bridge-bonded CO at edge sites [63, 64]. Three sharp peaks at 1630 cm^{-1}, 1425 cm^{-1}, and 1220 cm^{-1} are assigned to surface bicarbonate species on the bulk oxides, while weaker peaks at 1568 cm^{-1} and 1340 cm^{-1} are attributed to formate species [65]. In contrast, the Pd/TiO_2 catalyst exhibited minimal molecular adsorption, consistent with the SMSI effect discussed previously. The CO adsorption behavior on Pd/TiO_2 is influenced by the TiO_2 crystal phase (anatase or rutile) and pretreatment conditions. According to Zhou et al., Ru/Anatase-TiO_2 catalysts subjected to air annealing at 400 ℃ and H_2 reduction at 300 ℃ showed no distinct CO peaks in DRIFTS spectra, whereas rutile-TiO_2 or differently treated anatase-TiO_2 catalysts showed varied performance [66]. In our case, the catalyst is based on anatase-TiO_2 (confirmed by XRD results), and the air calcination and pre-treatment in an oxygen-rich environment resemble the conditions used in Zhou's study, explaining the absence of distinct CO peaks. However, Mn incorporation significantly altered the surface adsorption properties of Pd/TiO_2, leading to the emergence of IR peaks at 2085 cm^{-1}, 1630 cm^{-1}, and 1568 cm^{-1}. The 2085 cm^{-1} peak corresponds to linear CO adsorption on Pd^0, consistent with the Pd3d XPS results showing increased Pd^0 content upon Mn doping. A small peak at 2170 cm^{-1} is attributed to CO adsorption on Pd ions [67, 68]. Notably, a negative peak around 1340 cm^{-1} was observed, indicating desorption of CO_2 originally adsorbed from air on the fresh catalyst. Based on the CO-DRIFTS results, CO is predominantly adsorbed on both Pd and the support surface in the case of Pd/ZrO_2, whereas TiO_2-supported catalysts show limited CO adsorption on Pd. ZrO_2 is known to act as an oxygen supplier due to its high oxygen mobility, which significantly enhances CO adsorption also on the ZrO_2 support [69, 70]. In contrast, the TiO_2 surface has a higher oxygen density and forms stronger metal-support interactions, which suppress CO adsorption on Pd sites [44]. The addition of Mn modifies the oxygen structure and electronic structure, which has been confirmed by XPS results and discussed in previous sections, therefore enhanced surface adsorption properties.

Building on the CO-DRIFTS results, a similar trend can be suggested for the hydrogen spillover behavior. According to the mechanism of hydrogen spillover, hydrogen molecules dissociate on active metal sites and subsequently migrate onto the support surface. The SMSI of Pd/TiO_2 limits the surface adsorption and migration of hydrogen species. However, combining XPS results reveals that TiO_2-supported catalysts contain metallic Pd species. Mn doping further increases the proportion of metallic Pd and optimizes the electronic structure and surface oxygen structure of the catalyst , thereby enhancing the storage and migration of hydrogen atoms on the surface. In Pd/ZrO_2, hydrogen spillover is facilitated by the oxygen-rich nature of the support, which allows for greater accommodation of hydrogen atoms.

View Article Online
DOI: 10.1039/D5TA00854A

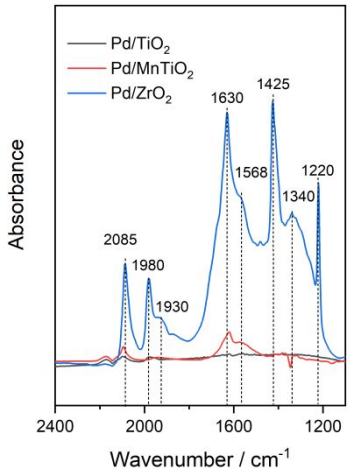

Fig. 3. CO DRIFTS spectra performed on pre-treated 1 wt% Pd/TiO_2, 1 wt% $Pd/MnTiO_2$, and 1 wt% Pd/ZrO_2 catalysts.

***In-situ* DRIFT study of NO-H_2**

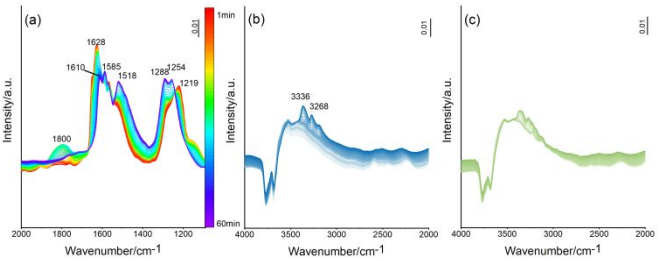

Fig. 4. *In-situ* DRIFTS spectra for Pd/ZrO_2 catalyst exposed to 2000 ppm H_2 for 1 h after flowing 500 ppm NO for 1 h in the region (a) 1100-2000 cm^{-1} and (b) 2000-4000 cm^{-1}; (c) 2000 ppm H_2 exposure for 1 h after flowing 500 ppm NO + 1% H_2O within region of 2000-4000 cm^{-1}.

In-situ DRIFTS studies of NO reduction by H_2 over the Pd/ZrO_2 catalyst were performed to investigate the surface-adsorbed species and intermediates involved in the reaction. From the CO DRIFTS data, there were less adsorbed species observed on TiO_2-supported catalysts; therefore, Pd/ZrO_2 was selected for this study. The detailed experimental procedure is described in **the Characterization methodology**. **Fig. 4a** illustrates the DRIFTS spectrum following H_2 introduction after NO adsorption under dry conditions, covering a 60-minute reaction period. At the initial stage, prominent bands appear at 1628 cm^{-1} and 1219 cm^{-1}, corresponding to bridged nitrates and weakly adsorbed NO_2^- species, respectively [71-75]. After approximately 30 min of H_2 exposure, a new band emerges at 1800 cm^{-1}, which gradually diminishes over time. This band is attributed to nitrosyl species (NO-metal), previously identified as key reactive intermediates in the H_2-SCR pathway [76]. The transient nature of this band indicates that nitrosyl species are formed on Pd sites and subsequently consumed during the reaction. Notably, this feature is absent under wet conditions, as shown in **Fig. S6b**, indicating that water inhibits the formation of nitrosyl species. This inhibition can be attributed to the competitive adsorption of water molecules on Pd active sites, which suppresses NO adsorption and thus hinders the formation of NO-metal nitrosyl intermediates. As H_2 exposure continues for 60 min, additional peaks appear at 1610 cm^{-1}, 1585 cm^{-1}, 1518 cm^{-1}, 1288 cm^{-1}, and 1254 cm^{-1}, suggesting the formation and transformation of various surface nitrate species. The peaks at 1585 cm^{-1}, 1518 cm^{-1}, 1288 cm^{-1}, and 1254 cm^{-1} are assigned to monodentate and bidentate nitrates, which could accumulate stably on the surface [71, 73, 75, 77]. Additionally, the band at 1610 cm^{-1} is attributed to adsorbed H_2O [5, 78]. **Fig. S6a** shows NO adsorption under wet conditions. Upon water addition, the surface nitrate species are altered, with bridged nitrates converting into bidentate nitrates. Thus, the presence of water promotes the transformation of NO_x species into more stable nitrate species rather than reactive nitrosyl intermediates. The peak at 1292 cm^{-1} becomes significantly more intense compared to dry conditions (**Fig. S6b** and **Fig. 4a**) and shifts from 1288 cm^{-1}, indicating a more uniform adsorption configuration and stronger bond, stabilized by the presence of water.

In the high wavenumber region of 2000–4000 cm^{-1} (**Fig. 4b** and **Fig. 4c**), the broad O-H stretching vibrations from water are found, and show a more significant increase with dry conditions with the time (blue) compare to the wet condition (green). Apart from that, two sharp bands appear at 3336 cm^{-1} and 3268 cm^{-1}, which are characteristic of NH_3 adsorption on Lewis acid sites [74, 77, 79]. It is important to note that H_2-SCR inherently generates water, and under conditions of additional water co-feeding, these NH_3-related peaks become significantly broader and less distinct (**Fig. 4c**). This implies that NH_3 formation is inhibited under wet conditions, likely due to competitive adsorption effects. Such inhibition may also contribute to the observed suppression in overall H_2-SCR activity in the presence of water.

Activity performance

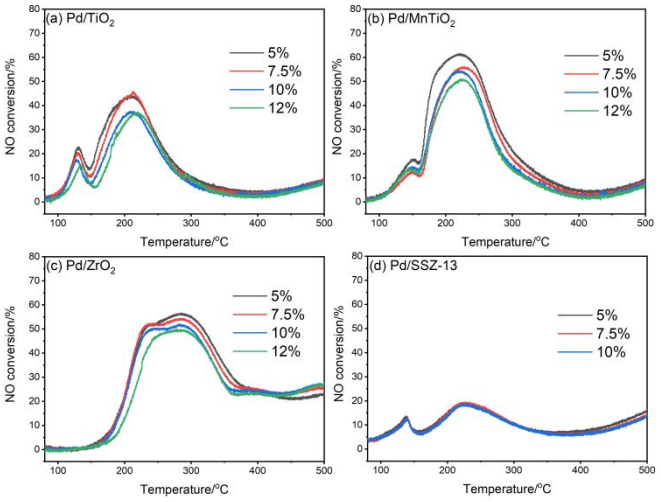

View Article Online
DOI: 10.1039/D5TA09954A

Fig. 5. NO conversion profiles with varying water content for (a) 1 wt% Pd/TiO_2 (b) 1 wt% $Pd/MnTiO_2$ (c) 1 wt% Pd/ZrO_2 (d) 1 wt% Pd/SSZ-13 catalysts (GHSV=20,000 h^{-1}(STP); gas inlet: 500 ppm NO, 5000 ppm H_2, 10% O_2, and 5/7.5/10/12% H_2O balanced in Ar; 80-500 ℃ with heating rate of 5 ℃/min).

The NO conversion and N_2 selectivity of the catalysts with different supports were evaluated by flow reactor cycle tests. The water content was gradually increased (5%/7.5%/10%/12%), except for Pd/SSZ-13, which was examined for 5%/7.5%/10% H_2O. Each cycle was repeated four times. All data presented in **Fig. 5** were extracted from the fourth cycle. Among all the samples, the SSZ-13-supported Pd catalyst showed minimal inhibition by water at concentrations between 5% to 10% (**Fig. 5d**). **Fig. S7** compares the performance of Pd/SSZ-13 for H_2-SCR in anhydrous and 5% water conditions. N_2 was measured by mass spectrometry, while other gases were analyzed by IR spectroscopy. The overall trends were similar in both environments. However, the NO consumption peak at around 240 ℃ was suppressed in the presence of water, accompanied by a small reduction in N_2 production. The results show that while water inhibits reactivity on Pd/SSZ-13, further increases in water content do not significantly affect performance (**Fig. 5d**). It is well-known that water will easily adsorb in zeolites, for example from PNA studies [80]. Moreover, NO adsorption is reduced in the presence of water for Pd/SSZ-13 [80]. These results are in line with our results where a decline in SCR activity is observed when adding water. However, when increasing the water concentration, no further water inhibition is observed. It is likely that 5% H_2O is sufficient to saturate the zeolite pores, which may explain the absence of any further decrease in activity at higher water contents.

Compared to the zeolite-supported catalyst, the Pd on metal oxides exhibited much higher activity for H_2-SCR (**Fig. 5a-c**). This enhancement is likely, at least partly, due to differences in the oxidation states of Pd. Under 5% water conditions, the maximum NO conversion reached 56% for Pd/ZrO_2, 44% for Pd/TiO_2, while 61% for $Pd/MnTiO_2$. From a water resistance perspective, increasing the water content from 5% to 12% led to a clear decline in reactivity. For Pd/TiO_2, the maximum NO conversion dropped from 44% to 36%, with a corresponding temperature shift of approximately 5 °C. Although Pd/ZrO_2 showed a smaller decrease from 56% to 50%, a shift toward higher temperatures was also observed, showing reduced catalytic activity. $Pd/MnTiO_2$ exhibited a decrease in maximum NO conversion from 61% to 50%. **Fig. S8** shows the data from all cyclic reaction tests (four cycles per condition) for the three oxide-supported catalysts. For Pd/TiO_2, NO conversion progressively declined with each cycle and increasing water content, indicating its instability under humid conditions. However, after the addition of Mn, the catalyst exhibited quite stable performance once the water content reached 10%, with only a slight drop. In the case of Pd/ZrO_2, the reaction performance remained quite similar across all four cycles under each water content condition, demonstrating good cyclic stability. Nevertheless, a clear inhibitory effect of water was observed as increased humidity reduced overall catalytic activity. This inhibition arises from the competitive adsorption of water molecules on Pd active sites, which hinders the adsorption and activation of NO and H_2 [81]. Possibly, this also weakens the H spillover effect by reducing H_2 activation.

Interestingly, all catalysts except Pd/ZrO_2 have two characteristic NO conversion peaks: a small one at lower temperatures and a larger one at higher temperatures, and a relatively low activity temperature range of about 80-150 ℃, which was described as 'volcano-shape'. Peng and his colleagues introduced aluminum as a promoter into the $Pd/CeZrO_4$ support, resulting in enhanced activity, explained by increased hydrogen spillover[19]. Based on previous characterizations, Pd/ZrO_2 and $Pd/MnTiO_2$ exhibited greater hydrogen spillover compared to Pd/TiO_2. The higher dispersion and smaller particle size of Pd in Pd/ZrO_2 and $Pd/MnTiO_2$ relative to Pd/TiO_2 may also contribute to their superior catalytic activities. $Pd/MnTiO_2$ exhibits an attenuated SMSI effect, which results in a higher proportion of metallic Pd species, more active for H_2 activation. Additionally, the presence of multivalent Mn creates a highly tunable electronic environment that modifies surface properties, further enhancing the H migration[82, 83].

Although the enhancement of hydrogen spillover and the improved dispersion of Pd particles both contribute to higher overall catalytic activity, we propose that the two distinct NO conversion peaks observed over Pd/TiO_2 at different temperatures are related to the presence of different Pd species. In contrast, Pd/ZrO_2 does not exhibit a low-temperature peak. The presence of metallic Pd in TiO_2-based Pd catalysts is considered to play a key role in low-temperature activity. Moreover, $Pd/MnTiO_2$ also contains metallic Pd species, as evidenced by XPS results. Combined with the enhanced hydrogen spillover and improved Pd dispersion, this leads to an increased activity. The double-peak behavior observed over Pd/SSZ-13 is also attributed to different reaction sites, since Pd/SSZ-13 include both Pd particles as well as ion-exchanged Pd We propose that the low-temperature peak originates from ion-exchanged Pd species in the zeolite, which significantly promote NO adsorption[84].

Fig. S9 and **Fig. S10** show the effluent gas concentrations from the catalysts measured during H_2-SCR in the presence of 5% and 10% water. Although the zeolite-supported catalysts exhibited higher N_2 selectivity, the oxide-supported catalysts demonstrated greater overall activity and N_2 yield, indicating stronger potential for further development. As a result, cycle tests for the zeolite catalysts were conducted only up to a water content of 10%. At temperatures over 400 ℃, oxidation reactions occurred across all catalysts, with NO_2 becoming the main product. By examining the NO concentrations (black curves) in both figures, it is evident that the addition of Mn enhances NO conversion significantly and improves the catalytic activity. A comparison between $Pd/MnTiO_2$ and Pd/ZrO_2 reveals that $Pd/MnTiO_2$ produces N_2, NH_3, and N_2O within the active temperature range. Notably, Pd/ZrO_2 not only generates a small amount of NO_2 within the H_2-SCR temperature range but also produces significantly more NO_2 at

higher temperatures compared to the other catalysts, indicating its stronger oxidation capability.

Another observation can be made from a careful examination of the product formation profiles. Over $Pd/MnTiO_2$, the N_2 formation curves at water concentrations of 5% and 10% show only a small difference as the temperature increases, while the NH_3 formation is slightly suppressed. In contrast, over Pd/ZrO_2, increasing the water concentration from 5% to 10% leads to an increase in NH_3 formation in the temperature range of 200-300 ℃, accompanied by a concurrent decrease in N_2 formation. These results indicate that, during the H_2-SCR reaction over $Pd/MnTiO_2$, N_2 concentration remains more stable under high water concentrations. This behaviour suggests that the higher fraction of metallic Pd enhances H_2 dissociation, generating a larger number of active hydrogen atoms that can counteract the inhibitory effects of competitive water adsorption.

NH_3 was a prominent byproduct at around 230-250 ℃ from the $Pd/MnTiO_2$ catalyst at both 5% and 12% water feed (**Fig. S9b** and **Fig. S10b**). As is well known, ammonia can serve as an effective reducing agent for NO_x reduction [83, 85]. Therefore, the $Pd/MnTiO_2$ monolith was combined in series with a conventional NH_3-SCR monolith catalyst, containing Cu/SSZ-13, positioned downstream. Experiments were conducted under identical space velocity and reaction conditions. Since the total monolith volume was doubled, the total feed flow rate was also doubled to maintain the same space velocity. As shown in **Fig. 6**, the NO conversion was successfully enhanced, reaching a maximum of 78% at 230 ℃ with 5% water. This resulted in the formation of 148 ppm N_2 and 48 ppm N_2O, corresponding to an N_2 selectivity of 76%. These results indicate that the NH_3 generated by the upstream $Pd/MnTiO_2$ was completely consumed for NO_x reduction, leading to an approximately 20% improvement in NO conversion via NH_3-SCR over the Cu-based catalyst. However, when the water content was increased to 12%, catalytic activity was suppressed. The maximum NO conversion dropped from 78% to 62%, mainly due to the competitive adsorption of water on the active surface sites. This inhibited the H_2-SCR performance of the $Pd/MnTiO_2$ catalyst, reducing NH_3 generation and consequently lowering the NH_3-SCR efficiency of the downstream Cu catalyst.

Further optimization of this dual catalyst system could focus on improving the water tolerance and hydrogen spillover efficiency of the upstream $Pd/MnTiO_2$ catalyst, as well as enhancing spatial integration between the two components to maximize NH_3 utilization. This could further mitigate water inhibition and strengthen overall synergistic performance under high water vapor conditions.

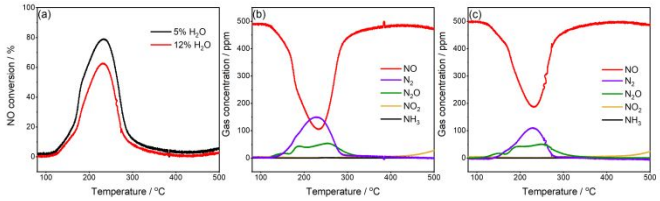

Fig. 6. $Pd/MnTiO_2$ and Cu/SSZ-13 monolith catalysts in series: (a) NO conversion profiles of 1 wt% $Pd/MnTiO_2$ + 2 wt% Cu/SSZ-13 with 5% water and 12% water contents and the effluent gas concentration profiles with (b) 5 % water, (c) 12% water (GHSV=20,000 h^{-1}(STP); gas inlet: 500 ppm NO, 5000 ppm H_2, 10% O_2, and 5/12 %H_2O balanced in Ar; T: 80-500 ℃ heating rate: 5 ℃/min)

Conclusions

This study compared the H_2-SCR performance of four catalysts: Pd supported on TiO_2, ZrO_2, SSZ-13, and Mn-doped TiO_2. Among these, the oxide-supported catalysts exhibited significantly higher catalytic activity than the zeolite-supported catalyst, with maximum NO conversions reaching 61% for $Pd/MnTiO_2$ and 56% for Pd/ZrO_2. However, in terms of water resistance, the zeolite-based catalyst outperformed the oxide-supported catalysts, which can be attributed to differences in the distribution of Pd species and the particle sizes on the supports. The inhibitory effect of water was confirmed by *in-situ* DRIFTS analysis, showing that the formation of active nitrosyl species and NH_3 was suppressed, while surface bidentate nitrate species were promoted in the presence of water. When the water content increased from 5% to 12%, the maximum NO conversion of $Pd/MnTiO_2$ decreased from 61 to 50%, yet the active temperature window remained almost unchanged. XPS measurements revealed a higher proportion of metallic Pd with Mn addition, along with an increased presence of low-valence Ti species, and a reduction in lattice oxygen content. These changes can lead to the formation of active oxygen vacancies or surface-adsorbed oxygen species. Specifically, Pd on the TiO_2 can have a strong SMSI effect which could explain the higher proportion of metallic Pd^0 species, which could enhance H_2 dissociation and migration, and improved hydrogen spillover. Additionally, we suggest that the high activity of Pd/ZrO_2 stemmed from good hydrogen storage and transfer capabilities due to its oxygen-rich property. The results indicate an increased hydrogen spillover for $Pd/MnTiO_2$ which could be due to the increased metallic Pd content, which can facilitate H_2 dissociation.

Analysis of the reaction products revealed that NH_3 was one of the main byproducts formed during the H_2-SCR process over $Pd/MnTiO_2$. To effectively utilize this byproduct, a downstream Cu-SSZ-13 monolith catalyst was introduced to establish a combined H_2-SCR and NH_3-SCR reaction system. This integrated configuration resulted in an enhanced maximum NO conversion of 78% under 5% water vapor conditions. Moreover, NH_3 was completely consumed, with N_2 and N_2O being the only detected products.

Conflicts of interest

There are no conflicts to declare

Data availability

Data for this article, including data for Supplementary Information are available at Zenodo at https://doi.org/10.5281/zenodo.18432637.

Acknowledgements

This study has been funded by the Swedish Energy Agency and carried out in collaboration with Volvo AB, Scania CV, and Johnson Matthey via a strategic vehicle research and innovation (FFI) project (P51458-1). We highly appreciate the technical support of the flow reactor from Lennart Norberg and Lasse Urholm. We also appreciate the resources for material characterizations from Chalmers Materials Analysis Laboratory at Chalmers.

Notes and references

1. R. D. Reitz, H. Ogawa, R. Payri, T. Fansler, S. Kokjohn, Y. Moriyoshi, A. Agarwal, D. Arcoumanis, D. Assanis, C. Bae, K. Boulouchos, M. Canakci, S. Curran, I. Denbratt, M. Gavaises, M. Guenthner, C. Hasse, Z. Huang, T. Ishiyama, B. Johansson, T. Johnson, G. Kalghatgi, M. Koike, S. Kong, A. Leipertz, P. Miles, R. Novella, A. Onorati, M. Richter, S. Shuai, D. Siebers, W. Su, M. Trujillo, N. Uchida, B. M. Vaglieco, R. Wagner and H. Zhao, *International Journal of Engine Research*, 2020, **21**, 3-10.
2. A. Onorati, R. Payri, B. Vaglieco, A. Agarwal, C. Bae, G. Bruneaux, M. Canakci, M. Gavaises, M. Günthner, C. Hasse, S. Kokjohn, S.-C. Kong, Y. Moriyoshi, R. Novella, A. Pesyridis, R. Reitz, T. Ryan, R. Wagner and H. Zhao, *International Journal of Engine Research*, 2022, **23**, 529-540.
3. J. M. Desantes, S. Molina, R. Novella and M. Lopez-Juarez, *Energy Conversion and Management*, 2020, **221**, 113137.
4. R. Rezaei, M. Sens, M. Riess and C. Bertram, in *Internationaler Motorenkongress 2021*, eds. J. Liebl, C. Beidl and W. Maus, Springer Fachmedien Wiesbaden, Wiesbaden, 2021, pp. 99-114.
5. M. Leicht, F. J. P. Schott, M. Bruns and S. Kureti, *Applied Catalysis B: Environmental*, 2012, **117-118**, 275-282.
6. E. Eßer, D. Schröder, A. V. Nartova, A. M. Dmitrachkov and S. Kureti, *Catalysis Letters*, 2022, **152**, 1598-1610.
7. J. Shao, P. H. Ho, D. Creaser and L. Olsson, *Applied Catalysis O: Open*, 2024, **188**, 206947.
8. G. Qi, R. T. Yang and L. T. Thompson, *Applied Catalysis A: General*, 2004, **259**, 261-267.
9. A. Ueda, T. Nakao, M. Azuma and T. Kobayashi, *Catalysis Today*, 1998, **45**, 135-138.
10. N. Macleod and R. M. Lambert, *Applied Catalysis B: Environmental*, 2002, **35**, 269-279.
11. M. Borchers, P. Lott and O. Deutschmann, *Top Catal*, 2023, **66**, 973-984.
12. K. Duan, B. Chen, T. Zhu and Z. Liu, *Applied Catalysis B: Environmental*, 2015, **176-177**, 618-626.
13. Z. Hu, X. Yong, D. Li and R. T. Yang, *Journal of Catalysis*, 2020, **381**, 204-214.
14. H. Shen, H. Li, Z. Yang and C. Li, *Green Energy & Environment*, 2022, **7**, 1161-1198.
15. M. M. Bettahar, *Catalysis Reviews*, 2022, **64**, 87-125.
16. P. Khatri and D. Bhatia, *Applied Catalysis A: General*, 2021, **618**, 118114.
17. H. Shin, M. Choi and H. Kim, *Physical Chemistry Chemical Physics*, 2016, **18**, 7035-7041.
18. L. Wang, H. Chen, M.-H. Yuan, S. Rivillon, E. H. Klingenberg, J. X. Li and R. T. Yang, *Applied Catalysis B: Environmental*, 2014, **152-153**, 162-171.
19. Z. Peng, Z. Li, Y.-Q. Liu, S. Yan, J. Tong, D. Wang, Y. Ye and S. Li, *Chem. Commun.*, 2017, **53**, 5958-5961.
20. Z. Geng, D. Wang, C. Zhang, X. Zhou, H. Xin, X. Liu and M. Cai, *International Journal of Hydrogen Energy*, 2014, **39**, 13643-13649.
21. S. Sterlepper, M. Fischer, J. Claßen, V. Huth and S. Pischinger, *Energies*, 2021, **14**, 8166.
22. D.-S. Ma and Z. Y. Sun, *International Journal of Hydrogen Energy*, 2020, **45**, 10580-10591.
23. C. N. Costa and A. M. Efstathiou, *Applied Catalysis B: Environmental*, 2007, **72**, 240-252.
24. C. N. Costa and A. M. Efstathiou, *J. Phys. Chem. C*, 2007, **111**, 3010-3020.
25. C. N. Costa, P. G. Savva, J. L. G. Fierro and A. M. Efstathiou, *Applied Catalysis B: Environmental*, 2007, **75**, 147-156.
26. C. Xu, W. Sun, L. Cao, T. Li, X. Cai and J. Yang, *Chemical Engineering Journal*, 2017, **308**, 980-987.
27. R. Burch, *Applied Catalysis B: Environmental*, 1999, **23**, 115-121.
28. R. Gui, Q. Yan, T. Xue, Y. Gao, Y. Li, T. Zhu and Q. Wang, *Journal of Hazardous Materials*, 2022, **439**, 129665.
29. K. G. Rappé, C. DiMaggio, J. A. Pihl, J. R. Theis, S. H. Oh, G. B. Fisher, J. Parks, V. G. Easterling, M. Yang, M. L. Stewart and K. C. Howden, *Emission Control Science and Technology*, 2019, **5**, 183-214.
30. Z. Li, M. T. Navarro, J. Martínez-Triguero, J. Yu and A. Corma, *Catal. Sci. Technol.*, 2016, **6**, 5856-5863.
31. P. H. Ho, D. Yao, D. Creaser and L. Olsson, *ACS Engineering Au*, 2022, **2**, 219-235.
32. A. Wang, P. Arora, D. Bernin, A. Kumar, K. Kamasamudram and L. Olsson, *Applied Catalysis B: Environmental*, 2019, **246**, 242-253.
33. A. Wang, M. Elena Azzoni, J. Han, K. Xie and L. Olsson, *Chemical Engineering Journal*, 2023, **454**, 140040.
34. J. Shao, P. H. Ho, W. Di, D. Creaser and L. Olsson, *Catal. Sci. Technol.*, 2024, **14**, 3219-3234.
35. S. Gates-Rector and T. Blanton, *Powder Diffr.*, 2019, **34**, 352-360.
36. Database of Zeolite Structures, 10.1002/9783527610761).
37. S. Tontisirin, in *Nanomaterials for Carbon Dioxide Capture and Conversion Technologies*, Elsevier, 2023, pp. 277-307.
38. P. Sudarsanam, A. Köckritz, H. Atia, M. H. Amin and A. Brückner, *ChemCatChem*, 2021, **13**, 1990-1997.
39. S. A. Yashnik, S. P. Denisov, N. M. Danchenko and Z. R. Ismagilov, *Applied Catalysis B: Environmental*, 2016, **185**, 322-336.
40. B. Karakurt, Y. Kocak, I. Lyubinetsky and E. Ozensoy, *J. Phys. Chem. C*, 2020, **124**, 22529-22538.
41. J. F. Moulder, W. F. Stickle, P. E. Sobol, J. Chastain and R. C. King Jr, *Perkin-Elmer Corporation*, 1992, **40**, 25.
42. P. Weerachawanasak, O. Mekasuwandumrong, M. Arai, S.-I. Fujita, P. Praserthdam and J. Panpranot, *Journal of Catalysis*, 2009, **262**, 199-205.

43. M.-S. Kim, S.-H. Chung, C.-J. Yoo, M. S. Lee, I.-H. Cho, D.-W. Lee and K.-Y. Lee, *Applied Catalysis B: Environmental*, 2013, **142-143**, 354-361.
44. S. J. Tauster, S. C. Fung and R. L. Garten, *Journal of the American Chemical Society*, 1978, **100**, 170-175.
45. C. Wang, Y. Li, C. Zhang, X. Chen, C. Liu, W. Weng, W. Shan and H. He, *Applied Catalysis B: Environmental*, 2021, **282**, 119540.
46. J. Li, G. Wu, N. Guan and L. Li, *Catalysis Communications*, 2012, **24**, 38-43.
47. S. Chakrabarti, S. Ginnaram, S. Jana, Z.-Y. Wu, K. Singh, A. Roy, P. Kumar, S. Maikap, J.-T. Qiu, H.-M. Cheng, L.-N. Tsai, Y.-L. Chang, R. Mahapatra and J.-R. Yang, *Sci Rep*, 2017, **7**, 4735.
48. H. Chen, T. Wu, X. Li, S. Lu, F. Zhang, Y. Wang, H. Zhao, Q. Liu, Y. Luo, A. M. Asiri, Z.-s. Feng, Y. Zhang and X. Sun, *ACS Sustainable Chemistry & Engineering*, 2021, **9**, 1512-1517.
49. B. Choudhury and A. Choudhury, *Current Applied Physics*, 2013, **13**, 1025-1031.
50. H. H. Nguyen, G. Gyawali and B. Joshi, *Journal of Ceramic Processing Research*, 2022, 33-40.
51. N. A. Merino, B. P. Barbero, P. Eloy and L. E. Cadús, *Applied Surface Science*, 2006, **253**, 1489-1493.
52. Y. Yang, Y. Jin, H. He and Z. Ye, *CrystEngComm*, 2010, **12**, 2663.
53. N. Kruse and S. Chenakin, *Applied Catalysis A: General*, 2011, **391**, 367-376.
54. H. Idriss, *Surface Science*, 2021, **712**, 121894.
55. M. Kaur, C. Sharma, N. Sharma, B. Jamwal and S. Paul, *ACS Appl. Nano Mater.*, 2020, **3**, 10310-10325.
56. H. Begum, M. S. Ahmed, D.-W. Lee and Y.-B. Kim, *Sci Rep*, 2019, **9**, 11051.
57. J. N. Bronsted, *Chem. Rev.*, 1928, **5**, 231-338.
58. H. Yu, C. Wang, X. Xin, Y. Wei, S. Li, Y. An, F. Sun, T. Lin and L. Zhong, *Nat Commun*, 2024, **15**, 5143.
59. Y. Zhou, J. Wang, L. Liang, Q. Sai, J. Ni, C.-t. Au, X. Lin, X. Wang, Y. Zheng, L. Zheng and L. Jiang, *Journal of Catalysis*, 2021, **404**, 501-511.
60. M. Filez, E. A. Redekop, V. V. Galvita, H. Poelman, M. Meledina, S. Turner, G. Van Tendeloo, A. T. Bell and G. B. Marin, *Physical Chemistry Chemical Physics*, 2016, **18**, 3234-3243.
61. G. Zhan and H. C. Zeng, *Nat Commun*, 2018, **9**, 3778.
62. R. B. Pace, T. M. Lardinois, Y. Ji, R. Gounder, O. Heintz and M. Crocker, *ACS Omega*, 2021, **6**, 29471-29482.
63. H.-Y. Chen, J. Lu, J. M. Fedeyko and A. Raj, *Applied Catalysis A: General*, 2022, **633**, 118534.
64. T. Lear, R. Marshall, J. Antonio Lopez-Sanchez, S. D. Jackson, T. M. Klapötke, M. Bäumer, G. Rupprechter, H.-J. Freund and D. Lennon, *The Journal of Chemical Physics*, 2005, **123**, 174706.
65. D. G. Rethwisch and J. A. Dumesic, *Langmuir*, 1986, **2**, 73-79.
66. J. Zhou, Z. Gao, G. Xiang, T. Zhai, Z. Liu, W. Zhao, X. Liang and L. Wang, *Nat Commun*, 2022, **13**, 327.
67. K. Mandal, Y. Gu, K. S. Westendorff, S. Li, J. A. Pihl, L. C. Grabow, W. S. Epling and C. Paolucci, *ACS Catal.*, 2020, **10**, 12801-12818.
68. R. Matarrese, L. Castoldi, S. Morandi, P. Ticali, M. C. Valsania and L. Lietti, *Applied Catalysis B: Environmental*, 2023, **331**, 122723.
69. Y. Guo, G. Lu, Z. Zhang, L. Jiang, X. Wang, S. Li, B. Zhang and J. Niu, *Catalysis Today*, 2007, **126**, 441-448.
70. D. Duprez, in *Studies in Surface Science and Catalysis*, eds. C. Li and Q. Xin, Elsevier, 1997, vol. 112, pp. 13-28.
71. L. Sivachandiran, F. Thevenet, A. Rousseau and D. Bianchi, *Applied Catalysis B: Environmental*, 2016, **198**, 411-419.
72. J. Watson, *Journal of Catalysis*, 2002, **210**, 295-312.
73. K. Hadjiivanov, V. Avreyska, D. Klissurski and T. Marinova, *Langmuir*, 2002, **18**, 1619-1625.
74. N. Macleod, R. Cropley and R. M. Lambert, *Catalysis Letters*, 2003, **86**, 69-75.
75. P. Savva and A. Efstathiou, *Journal of Catalysis*, 2008, **257**, 324-333.
76. T. J. Eldridge, M. Borchers, P. Lott, J.-D. Grunwaldt and D. E. Doronkin, *Catal. Sci. Technol.*, 2024, **14**, 4198-4210.
77. C.-H. Lin and H. Bai, *Applied Catalysis B: Environmental*, 2003, **42**, 279-287.
78. F. J. P. Schott, P. Balle, J. Adler and S. Kureti, *Applied Catalysis B: Environmental*, 2009, **87**, 18-29.
79. M. A. Centeno, I. Carrizosa and J. A. Odriozola, *Applied Catalysis B: Environmental*, 2001, **29**, 307-314.
80. A. Gupta, S. B. Kang and M. P. Harold, *Catalysis Today*, 2021, **360**, 411-425.
81. Z. Liu, J. Li and J. Hao, *Chemical Engineering Journal*, 2010, **165**, 420-425.
82. S. Mohan, P. Dinesha and S. Kumar, *Chemical Engineering Journal*, 2020, **384**, 123253.
83. M. Bendrich, A. Scheuer, R. E. Hayes and M. Votsmeier, *Applied Catalysis B: Environmental*, 2018, **222**, 76-87.
84. S. Yasumura, H. Ide, T. Ueda, Y. Jing, C. Liu, K. Kon, T. Toyao, Z. Maeno and K.-i. Shimizu, *JACS Au*, 2021, **1**, 201-211.
85. G. Qi, L. Wang and R. T. Yang, in *Urea-SCR Technology for deNOx After Treatment of Diesel Exhausts*, eds. I. Nova and E. Tronconi, Springer New York, New York, NY, 2014, pp. 149-177.

View Article Online
DOI: 10.1039/D6TA00954A

Dear Editors for *Journal of Materials Chemistry A* and *Materials Advances* ,

I confirm that the data supporting this study are available as described below.

The data herein includes the data collected and analyzed to support this study, including the data underlying the main text and the supplementary materials. All data have been packaged as a single dataset and deposited in the Zenodo repository. The dataset is publicly available at the following DOI: https://doi.org/10.5281/zenodo.18432637

Sincerely,

Louise Olsson (Corresponding author)

Chemical Engineering division，

Chalmers University of Technology

louise.olsson@chalmers.se